THE JOURNAL OF PHYSICAL CHEMISTRY LETTERS
A JOURNAL OF THE AMERICAN CHEMICAL SOCIETY

pubs.acs.org/JPCL Letter

Upconversion on the Micrometer Scale: Impact of Local Heterogeneity

Colette M. Sullivan,[†] Jia-Shiang Chen,[†] Xuedan Ma, Sarah Wieghold, and Lea Nienhaus*

Cite This: J. Phys. Chem. Lett. 2024, 15, 11869−11875 Read Online

ACCESS | Metrics & More | Article Recommendations | Supporting Information

ABSTRACT: The properties of perovskite/naphtho[2,3-*a*]pyrene (NaPy) upconversion devices are investigated by a combination of atomic force microscopy and photoluminescence mapping to understand the role of microscopic heterogeneity in the ensemble device properties. The results emphasize strong microscopic inhomogeneity across the perovskite/NaPy upconversion device due to local formation of NaPy microcrystals. NaPy shows emission from three distinct states in the solid state: S_1' emission at 520 nm, excimer emission at 560 nm, and S_1'' emission at 620 nm. Clear spatial differences in the emission spectrum under 405 nm excitation are found, highlighting that there is a strong microcrystal-to-microcrystal variation in the optical properties—emphasizing a need for multimodal measurements. Our results indicate that microcrystals with strong emission from the strongly coupled low-energy state S_1'' (J-dimer) show much higher upconversion intensity than those with dominant emission from the high-energy S_1' state (I-aggregate). Hence, our results suggest that microcrystals with strong emission from the low-energy state S_1'' act as isolated hotspots for upconversion.

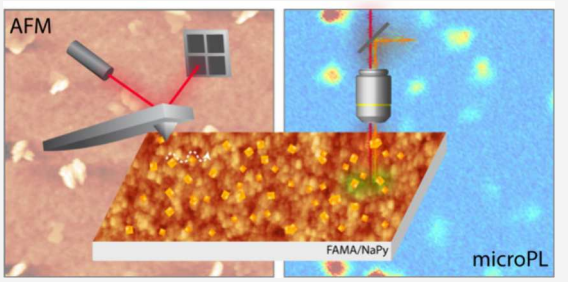

In photon upconversion (UC) via triplet−triplet annihilation (TTA), the energy of two spin-triplet states is combined in a spin-allowed Dexter-type exchange process to yield an excited spin-singlet state as well as a ground state, effectively resulting in the emission of a photon higher in energy than the two photons originally absorbed: an apparent anti-Stokes shift.[1−3] Since direct optical excitation of triplet states is a spin-forbidden process, triplet sensitizers are commonly utilized to achieve high triplet yields.[4−6] Several different triplet sensitization routes have been employed, including metal−organic complex-based sensitization,[4,7−10] exciton transfer from semiconductor quantum dots,[6,11] and perovskite nanocrystals.[12−16] In addition to these bound exciton-based triplet sensitization pathways, extraction of free charges at the bulk lead halide perovskite/organic semiconductor interface has shown to be a promising approach to form bound spin-triplet excitons in solid-state UC devices for a wide variety of polyaromatic hydrocarbons, e.g., rubrene,[17−20] 1-chloro-9,10-bis(phenylethynyl)anthracene,[21] and naphtho[2,3-*a*]pyrene (NaPy) (Figure 1a,b).[22]

Promising advances have been made with respect to understanding the mechanism and time scale of triplet generation at the perovskite/organic interface.[23,24] Here, triplet generation occurs on a subnanosecond time scale and triplets are formed by the independent transfer of a hole and electron and subsequent recombination to the bound triplet state.[23,24] However, the effects of local disorder and impact of the level of crystallinity, or local order and disorder, on TTA-UC have yet to be investigated in detail—which is particularly relevant in molecules such as NaPy, which possesses a strong drive for crystallization and limited solubility in the utilized solvent toluene. Previously, it has been shown that limited disorder enhances singlet fission in rubrene,[25] while the complete absence of order suppresses singlet fission.[26,27] Hence, it is also expected that order and disorder would have an impact on the reverse process of TTA-UC.

NaPy in the solid state shows emission from a several different states, which we had referred to as emission from S_1', excimer, and S_1'' (Figure 1b) in our initial study with emission features at 520, 560, and 620 nm, respectively.[22] The simple energy level diagram for perovskite-sensitized TTA-UC in NaPy based on the current state of knowledge shows the perovskite bandgap (1.55 eV), the 1.23 eV T_1 energy,[28] the triplet pair state ^{1}(TT) at 2.42 eV, and the emission from the excimer ^{1}D* (2.24 eV) and the respective states S_1' (2.38 eV) and S_1'' (2.00 eV).[22,29]

Our previous results indicated a strong dependence of the emission spectrum yield on the local environment of the molecule: amorphous, crystallite, or single crystal. In addition, stronger UC was found in regions with large NaPy crystallites.[22] A more in-depth investigation into the underlying cause of the different emissive states showed that depending on

Received: October 24, 2024
Revised: November 11, 2024
Accepted: November 13, 2024
Published: November 20, 2024

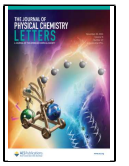

https://doi.org/10.1021/acs.jpclett.4c03075
J. Phys. Chem. Lett. 2024, 15, 11869−11875

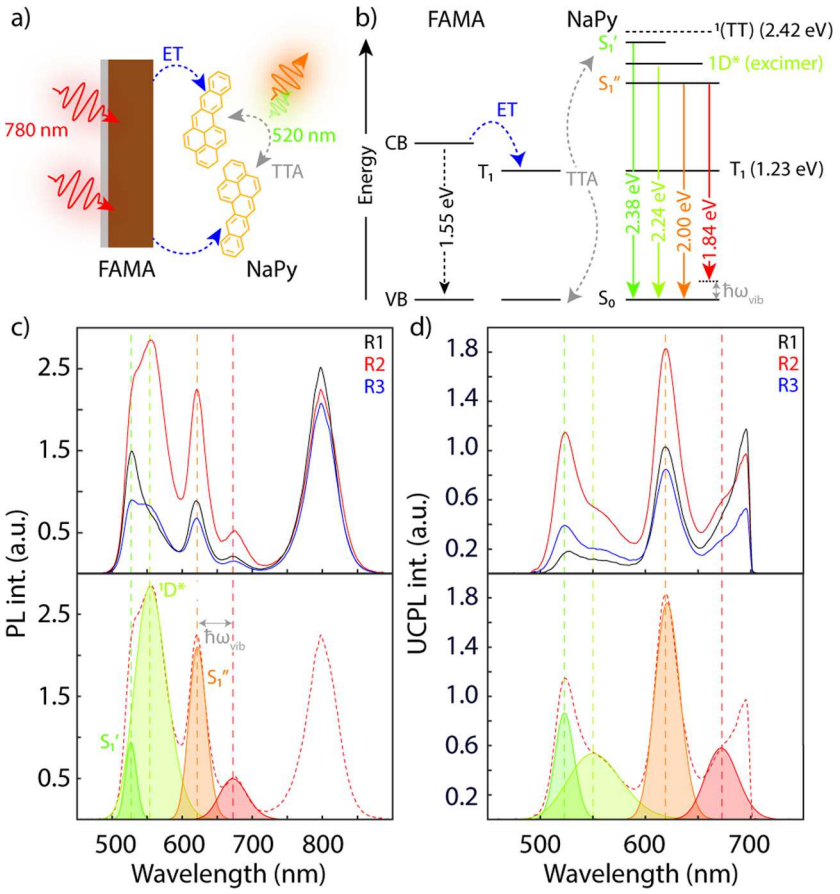

Figure 1. (a) FAMA/NaPy UC device schematic. (b) Energy level diagram for the FAMA/NaPy UC device. Several possible states can be populated via TTA-UC (S_1', the excimer ^{1}D*, and S_1''). (c) Top: Direct photoluminescence (PL) observed under 405 nm excitation across three representative regions for a FAMA/NaPy bilayer. Bottom: Gaussian fits to the underlying NaPy emission features. (d) UCPL of the bilayer at three representative locations under 780 nm excitation. Bottom: Gaussian fits to the underlying NaPy spectral features emphasizing that the same spectral features are present as under direct excitation, albeit with different intensities. The dashed lines are included as guides for the eye.

the monomer "concentration", which was used as a handle to influence the level of intermolecular interactions, the emissive state changed.[29] The NaPy emission features can be tuned from the monomeric emission, to excited state dimer or excimer emission (~555 nm), to an aggregate emission consistent with HJ coupling: a multidimensional I-aggregate as named by Caram and co-workers peaking at 520 nm.[30−32] With increasing concentration, the low-energy state S_1'' becomes more prominent, but no correlated absorption feature is found, indicating that similar to the excimer state, this low-energy emissive state is a purely excited-state phenomenon; hence, an aggregate-related feature can be ruled out as the origin. Conventional excimeric nature is unlikely due to the narrow emission line width and vibronic progression of the red-shifted feature. In addition, its longer-lived photoluminescence (PL) lifetime is at odds with the expected effect of strong J-type coupling in extended aggregates.[30] Therefore, the nature of the state points to a strongly coupled J-dimer, which we suggest can act as a hotspot for TTA-UC due to strong coupling priming the dimer for efficient and rapid TTA.[33,34]

To support the claim that the S_1'' state acts as a hotspot for TTA-UC, an understanding of the microscopic spatial distribution of optical properties is required. Even samples that appear homogeneous on the ensemble level (previously referred to as "amorphous" by Sullivan et al.[22]) show local discrepancies in their optical properties under direct excitation across a single sample. This local heterogeneity leads to strong differences in both the emission intensity and spectral shape across the 85% formamidinium (FA), 15% methylammonium (MA) lead triiodide ($FA_{0.85}MA_{0.15}PbI_3$, FAMA) FAMA/NaPy UC device (Figure 1c, three representative regions 1−3) under direct excitation at 405 nm showing both NaPy emission (500−700 nm) as well as the perovskite emission at ~800 nm. The ratio of the features corresponding to the two emissive states of NaPy varies for each measured representative location, as well as the intensity of the respective vibronic features.[22] Hence, there are clearly differences in the local environment which impact the ratio of the emitting species within our laser spot for the ensemble optical spectroscopy (~100 μm), despite the samples looking uniform to the eye.

Interestingly, the upconverted photoluminescence (UCPL) shows strong variations in the overall intensity across the bilayer UC device but much less change in the overall spectral shape based on the local region (Figure 1d, Figure S1). However, as previously reported, a change in the dominant emissive feature is found; emission primarily occurs from the low-energy state S_1'' (620 nm) after UC, while direct excitation favors emission from the higher-energy state S_1' at 520 nm.

To gain further insight into the UC process and role of local microscopic inhomogeneity on the properties of TTA-UC in FAMA/NaPy UC devices, we utilize a combination of atomic

https://doi.org/10.1021/acs.jpclett.4c03075
J. Phys. Chem. Lett. 2024, 15, 11869−11875

force microscopy (AFM) and microPL mapping to "zoom" into the microscale. In contrast to the ensemble optical spectroscopy shown in Figure 1c,d, where the emission is averaged across the laser spot size of ∼100 μm diameter of our instrument, this approach gives diffraction-limited information and can pinpoint whether individual NaPy crystals are primarily emitting from one state versus the other or whether there is a statistical distribution of the emissive states.

The 20 × 20 μm^2 AFM topography of the FAMA/NaPy bilayer is shown in Figure 2a where multiple micrometer-sized square NaPy microcrystals are clearly observed (Figure 2b), indicating a high level of drive for local molecular ordering during the growth of these microcrystals. No obvious change in the morphology and surface roughness of the underlying perovskite (Figure S2) is observed among the larger micrometer-sized NaPy crystals.

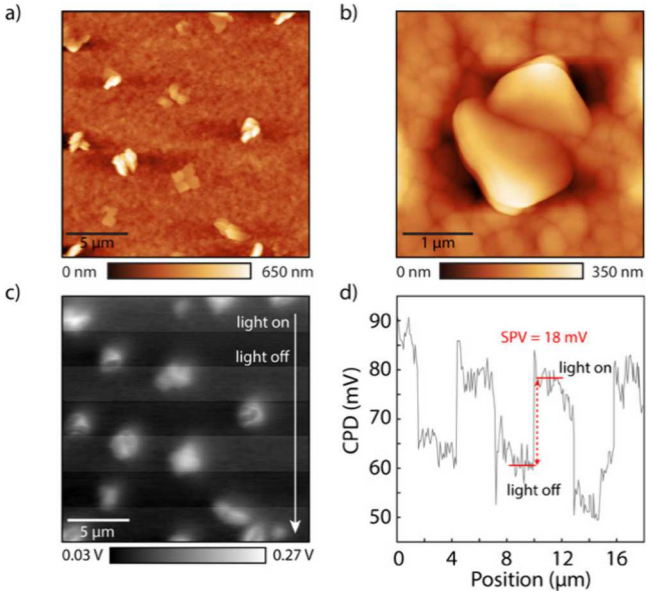

Figure 2. (a) AFM topography of the FAMA/NaPy bilayer showing the polycrystalline nature of the underlying perovskite film and the square NaPy microcrystals. (b) Zoom in on a single NaPy microcrystal. (c) KPFM image showing the CPD in the dark (darker regions) and under illumination (lighter regions). (d) Cross section of the CPD along the line shown in panel c to extract the SPV.

In a next step, Kelvin probe force microscopy (KPFM) is used to determine the changes in the surface potential upon deposition of the UC layer and during solvent treatment.[35,36] In general, KPFM can be used to map the spatial distribution of the contact potential difference (CPD) by applying a DC voltage to nullify the electrostatic force:

$$V_{CPD} = (\Phi_{tip} - \Phi_{sample})/-e \quad (1)$$

where Φ_{tip} and Φ_{sample} are the work function of the tip and sample, respectively.

For the pristine perovskite film, we find a relatively homogeneous CPD across the thin film surface. The expected n-type nature of the perovskite surface induced upon acetonitrile treatment is confirmed by the shift in the CPD to more negative values in comparison to the neat perovskite (Figure S3). This shift in the band bending behavior influences charge carrier extraction at the interface and will thus influence the rate and yield of triplet generation.[23] In the perovskite/NaPy hybrid bilayer, the CPD on the NaPy microcrystals shows a larger value (Figure 2c), indicating a lower value of the work function, i.e., a shallower Fermi energy in comparison to the perovskite.

KPFM measurements can be further used to determine the surface photovoltage (SPV) which is defined as the difference in the CPD in the dark and under steady-state illumination:

$$SPV = (CPD_{light} - CPD_{dark}) \quad (2)$$

The SPV can give information about the band bending near the surface in addition to the quasi-Fermi level splitting.[37] The CPD of FAMA becomes more positive under (white light)

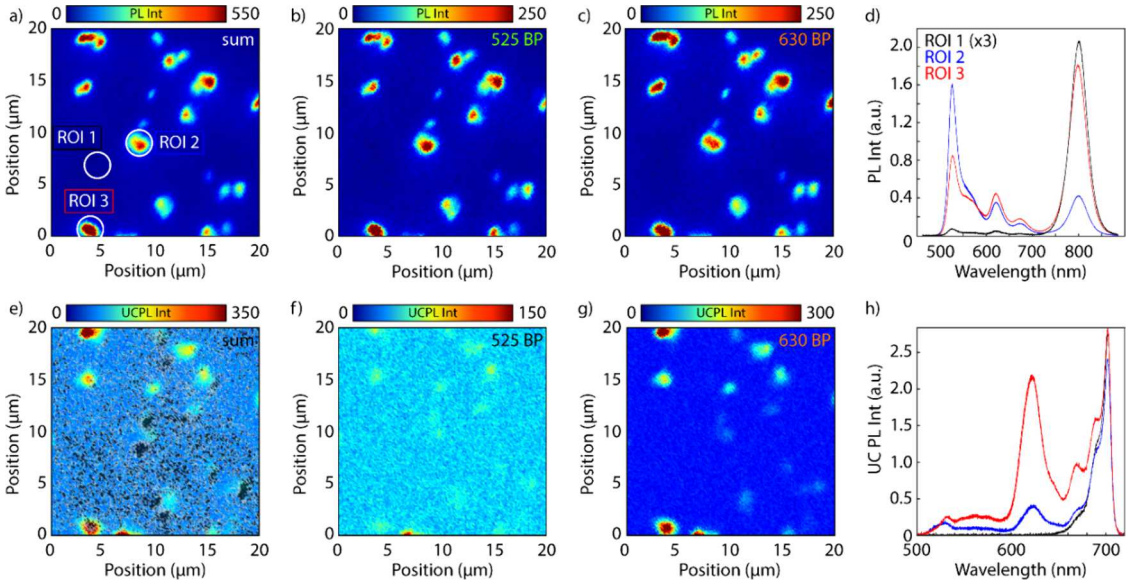

Figure 3. PL maps for the FAMA/NaPy bilayer collected under 405 nm excitation for the (a) total PL (sum of 525 and 630 BP), (b) 525 BP, and (c) 630 BP. (d) Direct excitation spectra collected at the three ROIs, as indicated in panel a. UCPL maps for bilayer collected under 780 nm excitation for the (e) total UCPL, (f) 525 BP, and (g) 630 nm BP. The ratio between the 525 and 630 BP direct PL (shown in panels b and c) has been included as a grayscale overlay in panel e; more gray indicates a higher fraction of S_1' emission. (h) UCPL spectra collected at the three ROIs.

https://doi.org/10.1021/acs.jpclett.4c03075
J. Phys. Chem. Lett. 2024, 15, 11869−11875

illumination (Figure 2c,d), and a change of 18 mV is observed between light on and off. Hence, the extracted SPV confirms our previous report that the perovskite exhibits n-type doping and upward band bending occurs at the surface, facilitating hole extraction, which is the first step in triplet generation at the perovskite/organic interface.[23,37]

Since the CPD value for NaPy is higher than that of the underlying perovskite, we can use the CPD to confirm the presence of smaller NaPy nanocrystallites between the large microcrystals (Figure S2), indicating that not all NaPy molecules are found in the larger microcrystals. Rather we have several different microscopic environments of the NaPy: nanocrystallites and microcrystals (*vide infra*). We had previously observed that different local environments tune the amount of emission from the low-energy state. However, this was observed on a macroscopic level, comparing thin films to macroscopic crystallites and single crystals. An interesting question presents itself: is there a spatial variation of the emission spectrum on the microscale? Or in other words: how uniform are the optical properties of the thin film truly?

To address this question and compare the AFM topography with the optical properties on the micrometer scale, integrated PL intensity micrographs (20 × 20 μm^2) are shown in Figure 3a under direct excitation at 405 nm, a wavelength that excites both the perovskite and NaPy directly. In agreement with the AFM topographies, local hotspots of NaPy emission are found corresponding to the location of the NaPy microcrystals, while only weak fluorescence is found in between microcrystalline regions, stemming from the NaPy nanocrystallites and possibly isolated NaPy molecules or a thin amorphous layer of NaPy coating the underlying perovskite grains. To emphasize the difference of the high-energy and low-energy emissive states (S_1' and S_1''), the NaPy PL is split into two channels using bandpass (BP) filters (Figure 3b,c) to isolate the individual emissive features and compare their relative intensities. PL spectra are extracted at three distinct regions of interest (ROIs) for comparison (Figure 3d): ROI 1, a region on the perovskite, which shows perovskite emission (~780 nm) and very weak NaPy emission, correlated to a region containing small amounts of NaPy between the observed microcrystals; ROI 2, a strongly emissive NaPy microcrystal with a high fraction of S_1' (525 BP) emission and lower perovskite PL intensity; ROI 3, a strongly emissive NaPy microcrystal with a comparatively low fraction of S_1' PL and strong emission from both the S_1'' state (630 BP) of NaPy and strong perovskite PL.

The corresponding total UCPL intensity under 780 nm excitation is highlighted in Figure 3e. For better comparison, the ratio of the direct PL intensity (*i.e.*, under 405 nm excitation) of S_1' and S_1'' is also overlaid on a grayscale (higher ratio: more S_1' PL, darker color), highlighting that the regions corresponding to strong S_1' PL are not highly TTA-UC active. Comparison of the UCPL intensity for S_1' and S_1'' (Figure 3f,g) emphasizes that TTA-UC is indeed more prominent in regions where rich emission from S_1'' is found and that even on the macroscopic scale UC is primarily observed from the lower-energy state.

Importantly, due to the obtained spatial distributions of the PL intensity of the two emissive states, we can conclude that the different emissive states are not related to surface/bulk emission of the microcrystals but rather their distribution is unique to the properties of the individual microcrystals. Investigation into a secondary 20 × 20 μm^2 region of the bilayer exhibits similar behavior (Figure S4).

The spectrally resolved UCPL spectra under 780 nm excitation collected at the same three ROIs as previously under direct excitation at 405 nm are shown in Figure 3h. In region of interest 1 (ROI 1), a region without microcrystals, we find no detectable TTA-UC. The two ROIs (ROI 2 and ROI 3) corresponding to the location of a microcrystal on the other hand display successful UC. However, ROI 2, the microcrystal with strong S_1' emission (520 nm) under direct excitation, shows only weak UC, whereas ROI 3, the microcrystal with a high intensity of S_1'' emission (620 nm) under direct excitation, demonstrates much more intense UCPL. No correlation of the UCPL intensity with the underlying perovskite PL intensity is found (compare Figure S5), indicating that the local perovskite quantum yield does not play a significant role in the obtained UCPL intensity.

Lastly, the recombination dynamics of each region of interest are investigated to determine whether the changes in the TTA-UC behavior are related to the microscopic NaPy recombination dynamics, e.g., caused by local defects. The corresponding PL decays for NaPy S_1' and S_1'' and the underlying FAMA are shown in Figure 4, and the

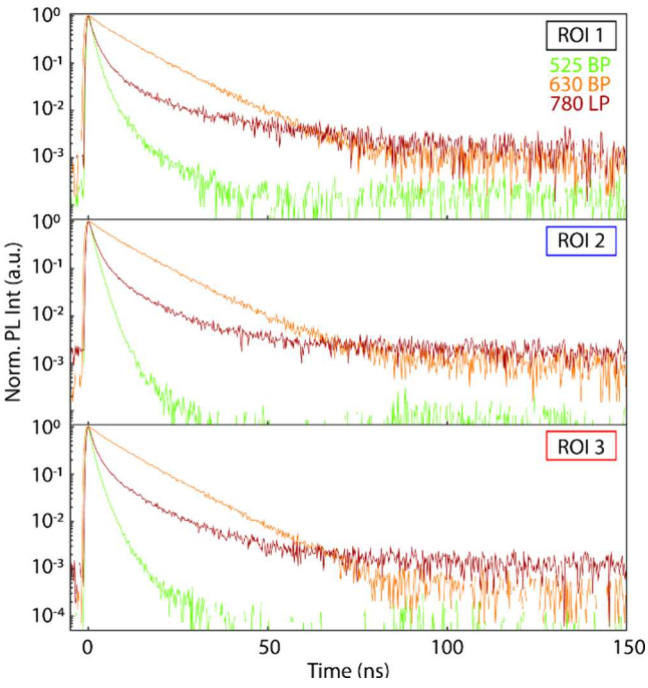

Figure 4. Bilayer PL decays for the three ROIs (ROI 1, top; ROI 2, middle; and ROI 3, bottom) collected under 405 nm pulsed excitation at 1 MHz and 0.6 W cm^{-2}. NaPy spectral features were isolated via 525 (green) and 630 BP (orange) filters, and a 780 LP (red) filter was used to isolate the underlying FAMA PL.

corresponding fit parameters are summarized in Table 1. Interestingly, no distinct differences are observed in the decays. The extracted PL lifetimes are comparable for each distinct spectrally resolved feature across the ROIs: S_1' (525/50 center/width BP), S_1'' (630/40 center/width BP), and the underlying perovskite (780 nm long-pass (LP)).

Hence, variations in the underlying kinetics across ROIs are not the cause of the differences in the upconversion properties. Rather, we conclude that the inherent population distribution of S1′ and S1″ states is important: regions with strong emission from S_1'' exhibit long lifetimes, strong coupling

https://doi.org/10.1021/acs.jpclett.4c03075
J. Phys. Chem. Lett. 2024, 15, 11869−11875

Table 1. Extracted Fit Parameters for NaPy and FAMA PL Decay Lifetimes for Each Region of Interest (ROI) and Each Spectral Region Determined by Bandpass (BP) and Long-pass (LP) Filters[a]

ROI	525/50 nm BP		630/40 nm BP	780 nm LP
Fit	$A\cdot\exp\left(\frac{-t}{\tau}\right)$	t^{-x}	$\sum_1^2 A_i\cdot\exp\left(-\frac{-t}{\tau_i}\right)$	$\sum_1^3 A_i\cdot\exp\left(-\frac{-t}{\tau_i}\right)$
1	1.4 ns	2.4 ns	9.3 ns	2.8 ns
2	1.6 ns	3.8 ns	9.6 ns	2.8 ns
3	1.3 ns	2.7 ns	9.2 ns	3.1 ns

[a]Amplitude-averaged weighted lifetimes are reported for biexponential and triexponential fits.

between molecules, and a favorable environment for efficient TTA-UC. On the other hand, regions with stronger emission from S_1' have a lower population of the strongly coupled S_1'' states available and a higher fraction of high-energy S_1' states which must be accessed through entropy or thermal energy following TTA-UC.[38] However, weaker electronic coupling between molecules may result in TTA-UC that is not efficient and other relaxation pathways are dominant instead.

In conclusion, we have investigated the microscopic properties of FAMA/NaPy UC devices by AFM and microPL. No detectable UC is found in the regions between microcrystals, a result that is unsurprising considering the low NaPy emission in this region under direct excitation. If TTA-UC occurs in this region, the generated singlet states are likely to be recycled back into the strongly broadband absorbing underlying perovskite due to their close proximity.[39] These results highlight that UC originates from only the ordered microcrystalline regions of NaPy. However, our results also indicate an excellent correlation between the population of the S_1' and S_1'' emissive states under direct excitation and the subsequent yield of TTA-UC. Regions with strong emission from S_1'' under direct excitation yields strong local UC. This result can be correlated to the local electronic coupling between molecules: stronger coupling can result in an increase in the rate of TTA-UC; in addition, there is a higher energetic driving force for formation of the singlet state from the triplet pair state ^{1}(TT).

Due to the reproducible strong ordering of NaPy into square microcrystals as indicated by the AFM topography, multiple crystal structures are not expected to be the underlying cause of the differences in the optical properties, and preliminary X-ray diffraction studies do not indicate the presence of multiple crystal structures but rather indicate a strong drive for preferential crystal plane orientation (Figure S6). To rationalize the differences in microcrystal performances, we therefore suggest that different amounts of molecular-level order and disorder within the crystal result in the observed changes in optical properties due to changes in the number of regions of strong coupling resulting in local J-dimers.[40] Furthermore, the low coverage of NaPy microcrystals on the underlying perovskite under the chosen fabrication conditions indicates that further device fabrication optimization by, e.g., vapor deposition could possibly push the achievable UC yields by increasing the surface coverage to boost charge extraction and TTA-UC active regions.

Looking beyond the immediate outcome of this study, these results emphasize the imminent need for multimodal measurement techniques that encompass a variety of simultaneous optical and structural methods. There is a clear structure–property relationship that cannot be ignored in solid-state devices and is overlooked in conventional ensemble spectroscopy. While we demonstrate similar observations independently by AFM and microPL mapping, we currently cannot correlate the resultant optical properties to a certain microcrystal morphology. However, a clear correlation of the optical properties of a single microcrystal and their respective shape, size, and height and electronic structure (based on I–V curves) bears great promise in providing valuable information about the microscopic properties and subsequent macroscopic properties of perovskite/organic interfaces.

■ ASSOCIATED CONTENT

Data Availability Statement

Raw data files are available at DOI: 10.17605/OSF.IO/VGZKD.

Supporting Information

The Supporting Information is available free of charge at https://pubs.acs.org/doi/10.1021/acs.jpclett.4c03075.

Normalized UCPL spectra, additional AFM and KPFM data, a second 20 × 20 μm^2 microPL map, perovskite PL map, and X-ray diffraction pattern for NaPy (PDF)

■ AUTHOR INFORMATION

Corresponding Author

Lea Nienhaus − *Department of Chemistry, Department of Materials Science and NanoEngineering, Department of Physics, and Rice Advanced Materials Institute, Rice University, Houston, Texas 77005, United States;* orcid.org/0000-0003-1412-412X; Email: nienhaus@rice.edu

Authors

Colette M. Sullivan − *Department of Chemistry, Rice University, Houston, Texas 77005, United States;* orcid.org/0000-0001-8660-4056

Jia-Shiang Chen − *Center for Nanoscale Materials, Argonne National Laboratory, Lemont, Illinois 60439, United States; Department of Materials Science and NanoEngineering, Rice University, Houston, Texas 77005, United States;* orcid.org/0000-0003-1612-3008

Xuedan Ma − *Center for Nanoscale Materials, Argonne National Laboratory, Lemont, Illinois 60439, United States; Department of Materials Science and NanoEngineering, Rice University, Houston, Texas 77005, United States;* orcid.org/0000-0002-3163-1249

Sarah Wieghold − *Advanced Photon Source, Argonne National Laboratory, Lemont, Illinois 60439, United States;* orcid.org/0000-0001-6169-3961

Complete contact information is available at: https://pubs.acs.org/10.1021/acs.jpclett.4c03075

Author Contributions

†C.M.S. and J.-S.C. contributed equally to this work.

Notes

The authors declare no competing financial interest.

■ ACKNOWLEDGMENTS

C.M.S. and L.N. acknowledge funding by the National Science Foundation under Grant No. DMR-2237977, the Camille and Henry Dreyfus Foundation (TC-23-050), and the Alfred P. Sloan Foundation. J.-S.C. and X.M. acknowledge support by

the National Science Foundation under Grant No. DMR-2421596. This project used resources provided by the X-ray Crystallography Center (FSU075000XRAY), the Materials Characterization Laboratory (FSU075000MAC) at the FSU Department of Chemistry and Biochemistry, and resources of the Advanced Photon Source, a U.S. Department of Energy (DOE) Office of Science user facility operated for the DOE Office of Science by Argonne National Laboratory under Contract No. DE-AC02-06CH11357. Work performed at the Center for Nanoscale Materials, a U.S. Department of Energy Office of Science User Facility, was supported by the U.S. DOE, Office of Basic Energy Sciences, under Contract No. DE-AC02-06CH11357.

REFERENCES

(1) Parker, C. A.; Hatchard, C. G.; Bowen, E. J. Delayed Fluorescence from Solutions of Anthracene and Phenanthrene. *Proc. R. Soc. London Ser. Math. Phys. Sci.* **1962**, *269* (1339), 574−584.
(2) Dexter, D. L. A Theory of Sensitized Luminescence in Solids. *J. Chem. Phys.* **1953**, *21*, 836−850.
(3) Monguzzi, A.; Tubino, R.; Meinardi, F. Upconversion-Induced Delayed Fluorescence in Multicomponent Organic Systems: Role of Dexter Energy Transfer. *Phys. Rev. B* **2008**, *77* (15), No. 155122.
(4) Schmidt, T. W.; Castellano, F. N. Photochemical Upconversion: The Primacy of Kinetics. *J. Phys. Chem. Lett.* **2014**, *5* (22), 4062−4072.
(5) Alves, J.; Feng, J.; Nienhaus, L.; Schmidt, T. W. Challenges, Progress and Prospects in Solid State Triplet Fusion Upconversion. *J. Mater. Chem. C* **2022**, *10* (20), 7783−7798.
(6) Mahboub, M.; Huang, Z.; Tang, M. L. Efficient Infrared-to-Visible Upconversion with Subsolar Irradiance. *Nano Lett.* **2016**, *16* (11), 7169−7175.
(7) Singh-Rachford, T. N.; Castellano, F. N. Pd(II) Phthalocyanine-Sensitized Triplet−Triplet Annihilation from Rubrene. *J. Phys. Chem. A* **2008**, *112* (16), 3550−3556.
(8) Arshad, A.; Castellano, F. N. Homomolecular Triplet−Triplet Annihilation in Metalloporphyrin Photosensitizers. *J. Phys. Chem. A* **2024**, *128* (36), 7648−7656.
(9) Monguzzi, A.; Tubino, R.; Meinardi, F. Upconversion-Induced Delayed Fluorescence in Multicomponent Organic Systems: Role of Dexter Energy Transfer. *Phys. Rev. B* **2008**, *77* (15), No. 155122.
(10) Monguzzi, A.; Tubino, R.; Meinardi, F. Multicomponent Polymeric Film for Red to Green Low Power Sensitized Up-Conversion. *J. Phys. Chem. A* **2009**, *113* (7), 1171−1174.
(11) Wu, M.; Congreve, D. N.; Wilson, M. W. B.; Jean, J.; Geva, N.; Welborn, M.; Van Voorhis, T.; Bulović, V.; Bawendi, M. G.; Baldo, M. A. Solid-State Infrared-to-Visible Upconversion Sensitized by Colloidal Nanocrystals. *Nat. Photonics* **2016**, *10* (1), 31−34.
(12) Mase, K.; Okumura, K.; Yanai, N.; Kimizuka, N. Triplet Sensitization by Perovskite Nanocrystals for Photon Upconversion. *Chem. Commun.* **2017**, *53* (59), 8261−8264.
(13) Chakkamalayath, J.; Kamat, P. V. Demystifying Triplet−Triplet Annihilation Mechanism in the CsPbI3−Rubrene−DBP Upconversion System. *J. Am. Chem. Soc.* **2024**, *146* (26), 18095−18103.
(14) Han, Y.; Luo, X.; Lai, R.; Li, Y.; Liang, G.; Wu, K. Visible-Light-Driven Sensitization of Naphthalene Triplets Using Quantum-Confined CsPbBr3 Nanocrystals. *J. Phys. Chem. Lett.* **2019**, *10* (7), 1457−1463.
(15) Luo, X.; Liang, G.; Han, Y.; Li, Y.; Ding, T.; He, S.; Liu, X.; Wu, K. Triplet Energy Transfer from Perovskite Nanocrystals Mediated by Electron Transfer. *J. Am. Chem. Soc.* **2020**, *142* (25), 11270−11278.
(16) Okumura, K.; Yanai, N.; Kimizuka, N. Visible-to-UV Photon Upconversion Sensitized by Lead Halide Perovskite Nanocrystals. *Chem. Lett.* **2019**, *48* (11), 1347−1350.
(17) Nienhaus, L.; Correa-Baena, J.-P.; Wieghold, S.; Einzinger, M.; Lin, T.-A.; Shulenberger, K. E.; Klein, N. D.; Wu, M.; Bulović, V.; Buonassisi, T.; Baldo, M. A.; Bawendi, M. G. Triplet-Sensitization by Lead Halide Perovskite Thin Films for Near-Infrared-to-Visible Upconversion. *ACS Energy Lett.* **2019**, *4*, 888−895.
(18) Wieghold, S.; Bieber, A. S.; VanOrman, Z. A.; Daley, L.; Leger, M.; Correa-Baena, J.-P.; Nienhaus, L. Triplet Sensitization by Lead Halide Perovskite Thin Films for Efficient Solid-State Photon Upconversion at Subsolar Fluxes. *Matter* **2019**, *1* (3), 705−719.
(19) Prashanthan, K.; Naydenov, B.; Lips, K.; Unger, E.; MacQueen, R. W. Interdependence of Photon Upconversion Performance and Antisolvent Processing in Thin-Film Halide Perovskite-Sensitized Triplet−Triplet Annihilators. *J. Chem. Phys.* **2020**, *153* (16), 164711.
(20) Wang, L.; Yoo, J. J.; Lin, T.-A.; Perkinson, C. F.; Lu, Y.; Baldo, M. A.; Bawendi, M. G. Interfacial Trap-Assisted Triplet Generation in Lead Halide Perovskite Sensitized Solid-State Upconversion. *Adv. Mater.* **2021**, *33* (27), 2100854.
(21) Sullivan, C. M.; Nienhaus, L. Recharging Upconversion: Revealing Rubrene's Replacement. *Nanoscale* **2022**, *14* (46), 17254−17261.
(22) Sullivan, C. M.; Nienhaus, L. Turning on TTA: Tuning the Energy Landscape by Intermolecular Coupling. *Chem. Mater.* **2024**, *36* (1), 417−424.
(23) Sullivan, C. M.; Bieber, A. S.; Drozdick, H. K.; M?ller, G.; Kuszynski, J. E.; VanOrman, Z. A.; Wieghold, S.; Strouse, G. F.; Nienhaus, L. Surface Doping Boosts Triplet Generation Yield in Perovskite-Sensitized Upconversion. *Adv. Opt. Mater.* **2023**, *11* (1), 2201921.
(24) Conti, C. R.; Bieber, A. S.; VanOrman, Z. A.; Moller, G.; Wieghold, S.; Schaller, R. D.; Strouse, G. F.; Nienhaus, L. Ultrafast Triplet Generation at the Lead Halide Perovskite/Rubrene Interface. *ACS Energy Lett.* **2022**, *7* (2), 617−623.
(25) Volek, T. S.; Armstrong, Z. T.; Sowa, J. K.; Wilson, K. S.; Bohlmann Kunz, M.; Bera, K.; Koble, M.; Frontiera, R. R.; Rossky, P. J.; Zanni, M. T.; Roberts, S. T. Structural Disorder at the Edges of Rubrene Crystals Enhances Singlet Fission. *J. Phys. Chem. Lett.* **2023**, *14* (50), 11497−11505.
(26) Finton, D. M.; Wolf, E. A.; Zoutenbier, V. S.; Ward, K. A.; Biaggio, I. Routes to Singlet Exciton Fission in Rubrene Crystals and Amorphous Films. *AIP Adv.* **2019**, *9* (9), No. 095027.
(27) Wieghold, S.; Bieber, A. S.; VanOrman, Z. A.; Rodriguez, A.; Nienhaus, L. Is Disorder Beneficial in Perovskite-Sensitized Solid-State Upconversion? Role of DBP Doping in Rubrene. *J. Phys. Chem. C* **2020**, *124* (33), 18132−18140.
(28) Aggarwal, N.; Patnaik, A. Dimeric Conformation Sensitive Electronic Excited States of Tetracene Congeners and Their Unconventional Non-Fluorescent Behaviour. *J. Chem. Sci.* **2019**, *131* (6), 52.
(29) Sullivan, C. M.; Szucs, A. M.; Siegrist, T.; Nienhaus, L. Naphtho[2,3-a]Pyrene Thin Films−H, I, or J? Aggregate Alphabet Soup Served over Triplet Pair States. *J. Phys. Chem. C* **2024**, *128*, 19248.
(30) Hestand, N. J.; Spano, F. C. Expanded Theory of H- and J-Molecular Aggregates: The Effects of Vibronic Coupling and Intermolecular Charge Transfer. *Chem. Rev.* **2018**, *118* (15), 7069−7163.
(31) Deshmukh, A. P.; Geue, N.; Bradbury, N. C.; Atallah, T. L.; Chuang, C.; Pengshung, M.; Cao, J.; Sletten, E. M.; Neuhauser, D.; Caram, J. R. Bridging the Gap between H- and J-Aggregates: Classification and Supramolecular Tunability for Excitonic Band Structures in Two-Dimensional Molecular Aggregates. *Chem. Phys. Rev.* **2022**, *3* (2), No. 021401.
(32) Deshmukh, A. P.; Koppel, D.; Chuang, C.; Cadena, D. M.; Cao, J.; Caram, J. R. Design Principles for Two-Dimensional Molecular Aggregates Using Kasha's Model: Tunable Photophysics in Near and Short-Wave Infrared. *J. Phys. Chem. C* **2019**, *123* (30), 18702−18710.
(33) Tian, D.; Qi, F.; Ma, H.; Wang, X.; Pan, Y.; Chen, R.; Shen, Z.; Liu, Z.; Huang, L.; Huang, W. Domino-like Multi-Emissions across Red and near Infrared from Solid-State 2-/2,6-Aryl Substituted BODIPY Dyes. *Nat. Commun.* **2018**, *9* (1), 2688.
(34) Musser, A. J.; Rajendran, S. K.; Georgiou, K.; Gai, L.; Grant, R. T.; Shen, Z.; Cavazzini, M.; Ruseckas, A.; Turnbull, G. A.; Samuel, I.

https://doi.org/10.1021/acs.jpclett.4c03075
J. Phys. Chem. Lett. 2024, 15, 11869−11875

D. W.; Clark, J.; Lidzey, D. G. Intermolecular States in Organic Dye Dispersions: Excimers vs. Aggregates. *J. Mater. Chem. C* **2017**, *5* (33), 8380−8389.
(35) Stranks, S. D. Multimodal Microscopy Characterization of Halide Perovskite Semiconductors: Revealing a New World (Dis)-Order. *Matter* **2021**, *4* (12), 3852−3866.
(36) Luchkin, S. Yu.; Akbulatov, A. F.; Frolova, L. A.; Tsarev, S. A.; Troshin, P. A.; Stevenson, K. J. Spatially-Resolved Nanoscale Measurements of Grain Boundary Enhanced Photocurrent in Inorganic CsPbBr3 Perovskite Films. *Sol. Energy Mater. Sol. Cells* **2017**, *171*, 205−212.
(37) Wieghold, S.; Tresback, J.; Correa-Baena, J.-P.; Hartono, N. T. P.; Sun, S.; Liu, Z.; Layurova, M.; VanOrman, Z. A.; Bieber, A. S.; Thapa, J.; Lai, B.; Cai, Z.; Nienhaus, L.; Buonassisi, T. Halide Heterogeneity Affects Local Charge Carrier Dynamics in Mixed-Ion Lead Perovskite Thin Films. *Chem. Mater.* **2019**, *31* (10), 3712−3721.
(38) Cheng, Y. Y.; Fückel, B.; Khoury, T.; Clady, R. G. C. R.; Ekins-Daukes, N. J.; Crossley, M. J.; Schmidt, T. W. Entropically Driven Photochemical Upconversion. *J. Phys. Chem. A* **2011**, *115* (6), 1047−1053.
(39) Wieghold, S.; Bieber, A. S.; VanOrman, Z. A.; Nienhaus, L. Influence of Triplet Diffusion on Lead Halide Perovskite-Sensitized Solid-State Upconversion. *J. Phys. Chem. Lett.* **2019**, *10*, 3806−3811.
(40) Chen, Y.; Lee, B.; Fu, D.; Podzorov, V. The Origin of a 650 nm Photoluminescence Band in Rubrene. *Adv. Mater.* **2011**, *23* (45), 5370−5375.

https://doi.org/10.1021/acs.jpclett.4c03075
J. Phys. Chem. Lett. 2024, 15, 11869−11875